Published in final edited form as:
Biochemistry. 2013 February 5; 52(5): 938–948. doi:10.1021/bi301476m.

Atomic structure of DUSP26, a novel p53 phosphatase

Ravi Kumar Lokareddy, **Anshul Bhardwaj**, and **Gino Cingolani***
Department of Biochemistry and Molecular Biology, Thomas Jefferson University, 233 South 10th Street, Philadelphia, Pennsylvania 19107

Abstract

Regulation of p53 phosphorylation is critical to control its stability and biological activity. Dual Specificity Phosphatase 26 (DUSP26) is a brain phosphatase highly overexpressed in neuroblastoma, which has been implicated in dephosphorylating phospho-Ser20 and phospho-Ser37 in the p53 transactivation domain (TAD). In this paper, we report the 1.68Å crystal structure of a catalytically inactive mutant (Cys152Ser) of DUSP26 lacking the first N-terminal 60 residues (ΔN60-C/S-DUSP26). This structure reveals the architecture of a dual-specificity phosphatase domain related in structure to *Vaccinia* virus VH1. DUSP26 adopts a closed conformation of the protein tyrosine phosphatase (PTP)-binding loop, which results in an unusually shallow active site pocket and buried catalytic cysteine. A water molecule trapped inside the PTP-binding loop makes close contacts both with main chain and side chain atoms. The hydrodynamic radius (R_H) of ΔN60-C/S-DUSP26 measured from velocity sedimentation analysis (R_H ~22.7 Å) and gel filtration chromatography (R_H ~21.0 Å) is consistent with a globular monomeric protein of ~18 kDa. Instead in crystal, ΔN60-C/S-DUSP26 is more elongated (R_H ~37.9 Å), likely due to the extended conformation of C-terminal helix α9, which swings away from the phosphatase core to generate a highly basic surface. As in the case of the phosphatase MKP-4, we propose that a substrate-induced conformational change, possibly involving rearrangement of helix α9 with respect to the phosphatase core, allows DUSP26 to adopt a catalytically active conformation. The structural characterization of DUSP26 presented in this paper provides the first atomic insight into this disease-associated phosphatase.

Keywords

DUSP26; MKP-8; Dual Specificity Phosphatase; p53; protein tyrosine phosphatase (PTP)-binding loop; dimerization

Dual-specificity phosphatases (DSPs) represent a heterogeneous subclass of the protein tyrosine phosphatase (PTP)-superfamily characterized by the unique ability to dephosphorylate both phospho-tyrosine and phospho-serine/threonine containing substrates (1–5). The first identified member of this family, VH1 is encoded by the *Vaccinia* virus H1 locus, which is conserved in all viruses of the *Poxviridae* family (6, 7). Since its identification in 1991 the number of VH1-like DSPs has quickly grown and, to date, it includes 61 members divided into 7 diverse subgroups (5). The human genome encodes 38 different VH1-like DSPs (5) (also referred to as 'DUSPs' (5)) that are essential cell signaling enzymes implicated in a multitude of physiological and pathological processes (5).

***Corresponding Author** Gino Cingolani, Department of Biochemistry and Molecular Biology, Thomas Jefferson University, 233 South 10th Street, Philadelphia, Pennsylvania 19107. gino.cingolani@jefferson.edu. Tel: (215) 503 4573; Fax: (215) 923 2117.

Author Contributions
The manuscript was written through contributions of all authors. All authors have given approval to the final version of the manuscript.

Similar to classical PTPs, DSPs contain a catalytic triad consisting of a Cys, an Arg and an Asp (8). Whereas the catalytic Cys and Arg are part of a phosphate-binding loop (or 'PTP-signature motif') that has consensus $Cys(X)_5Arg(Ser/Thr)$, the highly conserved Asp residue is located on a separate loop (known as 'general-acid loop'), near the top of the active site, usually 30–40 residues away from the active site motif in the primary sequence (8). DSPs share a similar catalytic mechanism as PTPs, characterized by the formation of a transient enzyme-phospho-substrate intermediate (1, 2). Unlike PTPs, DSPs have broader substrate specificity (9) and can also dephosphorylate non-peptidic substrates. Examples of DPSs specific to non-peptidic substrates include PTEN-like DSPs, that dephosphorylate D3-inositol phospholipids (10), PIR that dephosphorylates mRNA (11) and the glycogen phosphatase laforin (12). The high resolution structure of *Vaccinia* virus VH1, determined to 1.32 Å resolution (13, 14), as well as a wealth of other DSP structures determined over the past twenty years (8), have revealed that the DSP active site consists of a shallow, surface-exposed pocket, usually only ~6 Å in depth. This active site is simple and likely not sufficient to discriminate among the thousands of different phospho-substrates present, at any given time, in a living cell (3). Instead, substrate recognition and specificity are likely achieved by a dedicated tertiary/quaternary structural complementarity between the phosphatase and its target phospho-substrate.

DUSP26, also known to as MKP-8 (mitogen-activated protein kinase phosphatase-8 (15)), LDP-4 (low molecular-mass DUSP-4 (16)), or SKRP3 (stress-activated protein kinase pathway-regulating phosphatase) is a human DSP of the VH1-superfamily. DUSP26 is mainly expressed in neurons (17), retina (16, 18), heart (15, 17), adrenal gland (18) and skeletal muscle (15, 17, 18), where it localizes primarily to the cell nucleus (15, 16). Several potential substrates of DUSP26 have been identified. DUSP26 can function as a p38-specific phosphatase (15, 19) and an Erk-phosphatase (17), as well as, in PC12 cells, overexpression of DUSP26 was found to down-regulate the PI3K/Akt signaling pathway (18). Furthermore, several direct and indirect lines of evidence connect DUSP26 biology to tumorigenesis. First, DUSP26 inhibits p38-mediated apoptosis, thereby promoting anaplastic thyroid cancer cell growth and survival (19). Second, DUSP26 associates with and dephosphorylates Kap3, a component of the microtubule-directed protein complex KIF3, supporting a role in intracellular transport of β-catenin/N-cadherin (an established KIF3 cargo) and cell-cell adhesion (20). Finally, DUSP26 has been shown to directly bind to and dephosphorylate p53 transactivation domain (TAD) at Ser20 and Ser37, which results in repression of p53 transcriptional activity (21). DUSP26 expression is greatly unregulated in neuroblastoma cell lines, which, unlike many human cancer cells, maintain normal levels of wild type p53. Overexpression of DUSP26 suppresses p53 'onco-suppressive' function in response to genotoxic stress (21). For this reason, DUSP26 is a novel and promising target for the development of small molecule inhibitors for treatment of neuroblastoma and related pediatric malignancies. In this paper, we report a structural and biochemical characterization of human DUSP26. This work sheds light on the organization of a p53 phosphatase whose hyperactivation is linked to neuroblastoma.

EXPERIMENTAL PROCEDURES

Molecular biology and biochemical techniques

A synthetic gene encoding human DUSP26 was cloned in expression vector pET21b containing a C-terminal 6x histidine (6x-his) tag between restriction sites *NdeI* and *XhoI* (FL-DUSP26). Constructs lacking N-terminal residues 1–14 (ΔN14-DUSP26), 1–60 (ΔN60-DUSP26) and a core fragment spanning residues 61–187 (DUSP26-core) were generated by long PCR using FL-DUSP26 as template. ΔN60-C/S-DUSP26 and C/S-DUSP26-core were generated by site-directed mutagenesis of Cys152 to Ser. All DUSP26 constructs were expressed in *E. coli* BL21 (DE3)-RIL strain for 9 h at 25 °C after induction

with 0.4 mM IPTG at OD_{600} ~0.5. FL- and ΔN14-DUSP26 were completely insoluble, while constructs ΔN60-DUSP26, ΔN60-C/S-DUSP26, DUSP26-core and C/S-DUSP26-core were recovered in the soluble fraction. Soluble DUSP26 constructs were purified by immobilized metal affinity chromatography using TALON metal affinity resin (Clontech) followed by gel filtration chromatography on a Superdex 75 column 16/60 (GE Healthcare Life Sciences) in 150 mM sodium chloride, 20 mM HEPES pH 7.5, 5 mM β-mercaptoethanol, 0.1 mM PMSF. Purified DUSP26 constructs were concentrated to ~3 mg/ml using a 10K MWCO Vivaspin 15 concentrator (Sartorius). The Superdex 75 gel filtration column was calibrated using cytochrome C (12.4 kDa), carbonic anhydrase (29 kDa), albumin (66 kDa), alcohol dehydrogenase (150 kDa) and blue dextran (2,000 kDa) from the Gel Filtration Molecular Weight Markers Kit (Sigma). The hydrodynamic radius (R_H) of ΔN60-C/S-DUSP26 was determined by gel filtration chromatography (22) knowing the hydrodynamic radii of protein standards (23): cytochrome C, 17 Å; carbonic anhydrase, 23.6 Å; albumin, 35.5 Å; alcohol dehydrogenase, 45.5 Å.

In solution biophysical characterization

Circular dichroism (CD) spectra were recorded using a Jasco J-810 spectropolarimeter equipped with a Peltier temperature control system. Samples were measured in a rectangular quartz cuvette with a path-length of 1 cm at a final protein concentration of 10 μM in 20 mM HEPES (pH 7.0) and 150 mM NaCl at 20 °C. Temperature-induced unfolding of DUSP26 was monitored by recording variations in ellipticity at 222 nm as a function of temperature in 1.0 °C increments from 20 to 80 °C, as previously described (13, 24). Reversibility of unfolding was checked by slowly cooling unfolded DUSP26 to 20 °C followed by a second scan, which revealed DUSP26 unfolding is irreversible. The apparent melting temperature ($app T_m$) observed for ΔN60-C/S-DUSP26 and catalytically active ΔN60-DUSP26 was 69 °C and 68 °C, respectively, while for DUSP26-core, the $app T_m$ was 59 °C. To determine the oligomeric state of DUSP26 in solution, purified ΔN60-DUSP26, ΔN60-C/S-DUSP26 and C/S-DUSP26-core in 20 mM HEPES pH 7.0, 150 mM sodium chloride were analyzed in a Beckman Coulter ProteomeLab XL-1 analytical ultracentrifuge under velocity sedimentation mode. 400 μl of sample and 420 μl of reference buffer were loaded into separate compartments of a 12 mm path-length Epon centerpiece cell. Runs were performed at 40,000 rev min^{-1} and 20 °C. Absorbance values were collected at a wavelength of 278 nm using 5 – 100 μM protein samples. The data was fitted using a continuous sedimentation coefficient (c(s)) distribution model and an estimated molecular mass was obtained with the program SEDFIT (Peter Schuck, NIH http://www.analyticalultracentrifugation.com/download.htm). Both CD spectropolarimeter and analytical ultracentrifuge used in this study are part of the Kimmel Cancer Center X-ray Crystallography and Molecular Characterization shared resource facility, at Thomas Jefferson University.

Crystallization, data collection and structure determination

Crystals of ΔN60-C/S-DUSP26 were obtained using the hanging drop vapor diffusion methods by mixing together 2 μl of gel filtration purified protein at 3 mg/ml with 1 μl of 0.15 M calcium acetate hydrate, 0.1 M sodium cacodylate trihydrate pH 6.5, 17% w/v polyethylene glycol 8,000, at 18 °C. Crystals appeared within a few hours and grew to a maximal length of ~150 μm in 3 days. ΔN60-C/S-DUSP26 crystals were harvested in nylon cryo-loops and using 30% glycerol as cryoprotectant and flash-frozen in liquid nitrogen. Diffraction data were collected at beamlines X6A and X29 at the National Synchrotron Light Source (NSLS) on ADSC Quantum Q270 and Quantum-315r CCD detectors, respectively. Data indexing, integration and scaling were carried out with the HKL2000 software package (25). The asymmetric unit contains four copies of ΔN60-C/S-DUSP26 arranged into two dimers (referred to as protomers A, B, C and D) and ~42% solvent content. The structure of ΔN60-C/S-DUSP26 was solved by molecular replacement using an

ensemble search model containing the DSP-core of phosphatases VH1 (pdb 3CM3) and DUSP27 (pdb 2Y96), as implemented in PHASER (26). This initial phasing model was subjected to rounds of manual rebuilding using the program COOT (27) followed by refinement with phenix.refine, from the PHENIX software suite (28) and Refmac (29), using cycles of positional and anisotropic B-factor refinement, enforcing torsional non crystallographic symmetry restraints. The final atomic model of ΔN60-C/S-DUSP26 has a R_{work}/R_{free} of 18.5/21.5%, calculated using all diffraction data between 10-1.68 Å resolution (Table 2). The test set for R_{free} calculation was defined using 3,540 randomly chosen reflections. The final atomic model of ΔN60-C/S-DUSP26 contains residues 61–211 for protomers A, B, C and 61–209 for protomer D plus 532 water molecules. All protomers contain an additional N-terminal methionine at position 60; at the C-terminus, protomers A, B contain two additional residues (Leu/Glu) and protomer C only one additional residue (Leu) from the cloning site. Stereochemistry was checked using PROCHECK (30): the final model has good geometry with r.m.s.d. from ideal bond and angle of 0.006 Å and 1.0°, respectively. The Ramachandran plot shows 95.5% of residues in the most favored regions, 4.5% of residues in additional allowed regions and no disallowed residues. Refinement and data collection statistics are summarized in Table 2.

Structure analysis

All ribbon diagrams and surface representations in the paper were prepared using the program Pymol (31). Non-linear Poisson-Boltzmann electrostatic calculations were performed using APBS Tools (32). Topological diagram was generated using PDBsum (33) and structural superimpositions were carried out in Coot (27). Interface surface area was analyzed using PISA server (34). Hydrodynamic radii were calculated from atomic coordinates using HYDROPRO (35). Atomic coordinates and experimental structure factors have been deposited in the Protein Data Bank (accession code: 4HRF).

RESULTS

Domain organization and stability of DUSP26

DUSP26 consists of 211 residues and has predicted M.W. of ~23,945 Da. Bioinformatics analysis of DUSP26 organization reveals a central DSP-core spanning residues 61–186 surrounded by two predicted N-terminal α-helices (helix α1, res. 5–14; α2, res. 40–58) and a C-terminal helix (α9, res 187–211) (Fig. 1A). Aiming at structural studies, we synthesized the gene encoding human DUSP26 and expressed it in bacteria fused to a C-terminal 6x-his-tag. Attempts to purify full length DUSP26 (FL-DUSP26) under native conditions, in the presence of non-ionic detergents, or fused to a large affinity tag were unsuccessful, due to the phosphatase marked insolubility. As the first 60 residues of DUSP26 are highly enriched in hydrophobic amino acids, we generated two N-terminally deleted constructs lacking either helix α1 (ΔN14-DUSP26) or both helices α1–α2 (ΔN60-DUSP26), as well as a minimal DUSP26-core (residue 61–198) spanning only the predicted phosphatase core (Fig. 1A). These constructs displayed different solubility when expressed in bacteria, and among them, only ΔN60-DUSP26 and to a lesser extent DUSP26-core could be purified under native conditions for biophysical analysis.

To assess DUSP26 conformational stability and determine how N- and C-terminal deletions destabilized the protein, we measured heat-induced denaturation by monitoring variations in ellipticity at 222 nm as a function of temperature (Fig. 1B, Table 1). ΔN60-DUSP26 was found to unfold irreversibly in a highly cooperative manner, with an apparent melting temperature ($app T_m$) of ~68 °C. Replacing the active site cysteine 152 to serine yielded an inactive phosphatase (ΔN60-C/S-DUSP26) less prone to aggregation in solution and of comparable thermal stability ($app T_m$ ~69 °C). Instead, the smaller DUSP26-core had

significantly reduced thermal stability (*app*T_m ~59 °C), consistent with the lack of structural determinants at both N- and C-termini. Thus, DUSP26 is a stable protein phosphatase; N- and C-terminal structural elements flanking the predicted DSP-core affect the enzyme stability likely by mediating intra- or inter-molecular interactions.

ΔN60-DUSP26 is monomeric in solution

DUSP26 oligomeric state was investigated in solution by analytical ultracentrifugation (AUC) sedimentation velocity analysis. As FL-DUSP26 was completely insoluble, we restricted our analysis to ΔN60-DUSP26 and DUSP26-core, which are soluble under physiological conditions. Fig. 2A shows a typical sedimentation profile of ΔN60-C/S-DUSP26 obtained in 20 mM HEPES pH 7.0, 150 mM sodium chloride, at 4°C. In a range of concentration between 5–100 μM, ΔN60-C/S-DUSP26 migrated as a homogeneous species characterized by a monophasic sedimentation boundary (Fig. 2A). This is indicative of a single major (>94.7%) component in solution migrating with an apparent sedimentation coefficient (s*) of 1.925S (Table 1). Conversion of the distribution of the apparent sedimentation coefficient to molecular mass revealed a M.W. ~18.1 ± 0.5 kDa, which agrees well with a monomer of ΔN60-C/S-DUSP26 (expected molecular mass ~18.2 kDa). Furthermore, the ΔN60-C/S-DUSP26 frictional ratio was *f/fo* ~1.23, consistent with a globular protein of hydrodynamic radius R_H ~22.7 Å (Table 1). Essentially identical hydrodynamic parameters were measured for ΔN60-DUSP26 (Table 1), confirming the active site mutation did not affect oligomerization. Finally, DUSP26-core was also monomeric in solution (sedimentation coefficient ~1.811S) and of globular shape (frictional ratio *f/fo* ~1.20) (Table 1), as expected for a minimal DSP core.

To validate the AUC data, we also investigated ΔN60-C/S-DUSP26 hydrodynamic properties by gel filtration chromatography using a Superdex 75 column. At physiological salt concentration, in a range of concentration between 5–100 μM, ΔN60-C/S-DUSP26 migrated as a monodisperse major peak, eluting after ~91 ml (Fig. 2B). Molecular weight calibration standards confirmed this elution volume is consistent with a ~20 kDa globular species of hydrodynamic radius R_H ~21.0 Å (Fig. 2B, Table 1). Thus, in contrast to VH1 (13, 14) and DUSP27 (36), ΔN60-C/S-DUSP26 adopts a monomeric conformation in solution.

Atomic structure of ΔN60-DUSP26

To shed light on the three-dimensional structure of DUSP26, we crystallized ΔN60-DUSP26 and ΔN60-C/S-DUSP26. As observed for VH1 (13), the active site mutant gave larger crystals that diffracted to 1.68 Å resolution using synchrotron radiation. The structure of ΔN60-C/S-DUSP26 was solved by molecular replacement and refined to a R_{work}/R_{free} of 18.5% and 21.5%, using all reflections between 10-1.68 Å resolution (Table 2). ΔN60-C/S-DUSP26 crystallized as a tetramer generated by two C-terminally swapped dimers (Fig. 3A) rotated by 180° in the crystallographic asymmetric unit. Each ΔN60-C/S-DUSP26 dimer is stabilized by helix α9, which is swapped between two protomers, thereby generating a compact structure of 60 Å in length and ~45 Å in width (Fig. 3A). Since ΔN60-C/S-DUSP26 is proven to be monomeric in solution, at physiological ionic strength and concentration (between 5–100 μM) (Fig. 2), the domain-swapped dimer seen in the asymmetric unit likely reflects a crystallographic artifact owed to the high protein concentration achieved during crystallization and the presence of precipitant. The tertiary structure of ΔN60-C/S-DUSP26 is illustrated in Fig. 3B. The protein resembles a ‘lollipop’, built by a globular DSP domain of ~40 Å in diameter connected to a 35 Å long C-terminal helix (α9), nearly orthogonal to the phosphatase core. The dual specificity phosphatase core (residues 61–187) (Fig. 3B,C) consists of a central five-stranded β-sheet (β1–β5) (highlighted in light blue in Fig. 3C) sandwiched between two clusters of three α-helices

(α3–α5 and α6–α8) that surround the central core and make contacts with the solvent. The last DSP-core helix, α8 connects to the long helix α9 (res 191–208), which is swapped between two subunits (Fig. 3A–C). This helix is significantly longer than in most DUSPs (20 residues versus 10–12) and presents several conserved basic and hydrophobic residues.

Architecture of DUSP26 active site

The 1.68 Å resolution structure of ΔN60-C/S-DUSP26 provides a detailed view of the enzyme active site. DUSP26 catalytic triad consists of Arg158, Asp120 and Cys152, which is replaced by a serine in our structure (Fig. 4A). The conformation adopted by the PTP-binding loop (PTP-loop) in DUSP26 renders the active site pocket very shallow, almost imperceptible by scanning the enzyme surface (Fig. 4B). The catalytic residue Cys152 (Ser152 in our structure) sits at bottom of the active site, buried ~7 Å below the enzyme surface, at a position that appears to have minimal solvent exchange. DUSP26 catalytic triad, residues Arg158, Asp120 and Cys152 are structurally superimposable to the catalytic triad of the prototypical VH1 (13) (Fig 5A), as well as of other VH1-related DUSPs such as VHZ (37) and DUSP27 (36) (*data not shown*). However, the orientation of DUSP26 PTP-loop between residues 153–157 deviates significantly from that seen in VH1. In DUSP26 residues 153–157 mainchain atoms are shifted ~3.5 Å upward compared to VH1 and the carbonyl groups of Val154 and Gly155 point down inside the active site, as opposed to project outwards as in VH1 (Fig. 5A). This backbone conformation is made possible by the fact that position 155 of DUSP26 PTP-loop is occupied by a glycine (as opposed to alanine as in VH1 (13)), which allows considerably greater mainchain flexibility due to the small van der Waals radius of its single hydrogen atom side chain. Interestingly, the closed conformation of DUSP26 PTP-loop resembles the conformation visualized crystallographically in the phosphatase MKP-4 (38). This protein also presents backbone carbonyl groups pointing into the active site and has minimal catalytic activity in the absence of substrate (33) (Fig. 5B). Furthermore, DUSP26 active site lacks a bulky phosphate (or sulfate) ion (as seen in VH1 (13) or DUSP27 (36)), but is occupied by a water molecule (referred to as 'active site Water' or 'W_{AS}') (Fig. 4A), visible as a ~3.5 σ peak in a Fo – Fc electron density difference map (Fig. 5C). This active site water molecule is coordinated by backbone atoms of PTP-loop residues 153–158 as well as it makes close contacts (2.9–3.0 Å) with side chain atoms of Arg158, Ser152 and Asp120 (Fig. 5C). Accordingly, the anisotropically refined B-factor of W_{AS} varies between 22.5–31.0 $Å^2$ in the four protomers present in the asymmetric unit, which is significantly lower than the average B-factor of both protein (36.9 $Å^2$) and solvent (~ 41.1 $Å^2$) atoms (Table 2), underscoring slow solvent exchange.

Evidence for a closed conformation of the C-terminal helix α9

To investigate the degree of structural conservation, we superimposed ΔN60-C/S-DUSP26 to the prototypical VH1, which we previously determined to 1.32 Å resolution (13) and whose crystallographic structure matches the conformation observed in solution (14). Despite the low sequence identity (~26%), the two phosphatases are structurally superimposable (rmsd ~1.92 Å), with 109 of 153 residues in DUSP26 topologically matched in VH1 (Fig. 6A). While the DSP-core is remarkably conserved, the position of DUSP26 C-terminal helix α9 is dramatically different from its counterpart in VH1, helix $α6_{VH1}$ (highlighted in red in Fig. 6A). In VH1, this helix adopts a closed conformation that packs against the DSP-core and engages in hydrophobic contacts with helix $α4_{VH1}$ (continuous to the PTP-loop) (Fig. 6A). In contrast, in our structure helix α9 swings 180° away from its DSP-core to make contacts with another subunit ('protomer B'), to which it is related by 2-fold non-crystallographic symmetry. Examination of the crystallographic domain swapped interface (Fig. 3A) (which, as previously demonstrated, represents a crystallographic artifact) reveals that helix α9 of protomer B ($α9_B$) (shown in gray in Fig. 6A) also packs

against the DSP-core of protomer A, occupying the same position as helix $\alpha 6_{VH1}$ in VH1. Thus, an inter-molecular contact between the DSP-core of ΔN60-C/S-DUSP26 protomer A and helix $\alpha 9_B$ mimics in our crystal structure the closed conformation of helix $\alpha 6_{VH1}$ generated intra-molecularly in VH1. Helix $\alpha 9_B$ also interacts with the general acid loop, mainly via electrostatic contacts between Asn191 (of protomer B) and Asp120 (of protomer A). This interaction does not perturb the conformation of DUSP26 general acidic loop, which is superimposable to its counterpart in VH1 (rmsd ~1.1 Å).

Next, we asked if the extended conformation of helix α9 seen in crystal is also populated in solution, or if this helix folds back onto its DSP-core to generate a globular structure similar to VH1 (13). To answer this question, we generated an atomic model of ΔN60-C/S-DUSP26 with helix α9 folded onto its DSP-core ('ΔN60-C/S-DUSP26-closed') to mimic the position occupied by helix $\alpha 9_B$ (or $\alpha 6_{VH1}$) (Fig. 6B). This model appears very plausible, as most of the hydrophobic residues mediating packing of helix $\alpha 6_{VH1}$ to its DSP-core are also conserved in DUSP26 helix α9 (shown by arrows in Fig. 6A). Accordingly, the hydrodynamic radius of ΔN60-C/S-DUSP26-closed calculated from atomic coordinates (R_H ~24.3 Å) is remarkably similar to ΔN60-C/S-DUSP26's R_H determined experimentally using velocity sedimentation analysis (R_H ~22.7 Å) and gel filtration chromatography (R_H ~21.0 Å) and strikingly smaller than the R_H measured from ΔN60-C/S-DUSP26 crystallographic coordinates (R_H ~37.9 Å) (Fig. 6B, Table 1). Thus, ΔN60-C/S-DUSP26 exists in solution in a conformation more globular than in crystal, likely due to a closed conformation of helix α9.

DISCUSSION

More than 50% of all human cancers have mutations or deletions in the p53 gene [24]. In neuroblastoma, an aggressive pediatric malignancy, p53 levels are mostly wild type but the protein is poorly active due to hypo-phosphorylation of its TAD, which is partially structured in solution (39). In the classical model of p53 activation, exposure to DNA-damaging agents and cytotoxic stress result in phosphorylation at several Ser and Thr in p53-TAD, which is important for p53 stabilization, DNA-binding and transcriptional activity (40–42). In particular, phosphorylation of Ser20 creates a phospho-SDLxxLL docking motif critical to the stabilization of the binding of the transcriptional co-activator p300 (43–45). Misregulation of p53-stabilization by dephosphorylation of its TAD is linked to chemoresistance in neuroblastoma and other cancers (46, 47). Hypophosphorylated p53 is in fact unstable and has reduced tumor suppressor function (40), which contributes to chemoresistance, tumor metastasis and poor patient survival (48–50). Shang *et al.* recently demonstrated that DUSP26 is highly overexpressed in neuroblastoma, where it represses p53 oncosuppressor function by specifically dephosphorylating pSer20 and pSer37 (21). Furthermore, high level of DUSP26 promotes resistance of human neuroblastoma to doxorubicin, a drug commonly used in cancer chemotherapy. As a corollary, inhibition of DUSP26 is a potential target to enhance p53-mediated response, which could be useful to treat neuroblastomas insensitive to chemotherapy and increase the success of treatment. The 1.68 Å crystal structure of ΔN60-C/S-DUSP26 presented in this paper provides the first atomic insight into this disease-associated phosphatase.

DUSP26 is a monomeric phosphatase

Dimerization is emerging as an important structural determinant for small dual specificity phosphatases, previously assumed to be monomeric. In at least three cases, dimerization has been shown to modulate phosphatase catalytic activity. Liu *et al.* demonstrated that laforin dimerization is essential for phospho-glycogen recognition and catalytic activity (51). Likewise, dimerization of the myotubularin (MTM)-related protein 2 (MTMR2) via a C-terminal coiled-coil was found to be essential for membrane association and

phosphoinositide dephosphorylation (52). Finally, we recently demonstrated that VH1 dimeric structure is essential for recognition and dephosphorylation of activated STAT1 (13, 14). The crystal structure of DUSP27 was also recently reported (36) and, as in VH1, this phosphatase also dimerizes via an N-terminal domain-swapped α-helix. In contrast, in this paper we provide compelling evidence that ΔN60-C/S-DUSP26 adopts a monomeric conformation in solution, in a range of concentration between 5–100 μM, likely close to the physiological concentration of DUSP26 in brain cells. Using sedimentation velocity analysis and gel filtration chromatography, we determined that ΔN60-C/S-DUSP26 exists in solution as a globular species of hydrodynamic radius R_H ~22.7/21.0 Å (Table 1). This conformation is different from the crystallographic structure, which is elongated due to the extended conformation adopted by helix α9. Structural comparison of ΔN60-C/S-DUSP26 with VH1 suggested that the extended conformation of helix α9 seen in crystal is stabilized by a crystallographic contact with another protomer (protomer B), which packs its helix $\alpha9_B$ against the DSP-core, mimicking the closed conformation seen in VH1 (Fig. 6A). Although this crystallographic packing results in an artificial dimeric structure (Fig. 3A) that is not observed in solution, the ability of helix α9 to swing by >180° around its DSP-core reflects the potential flexibility of this secondary structure element. Intriguingly, the extended conformation of helix α9 projects five basic residues to the solvent (Arg 192/196/203/204/206), all clustered on one side of the helix (Fig. 7). These residues generate a continuous basic surface that, together with four arginines from helix α4 (Fig. 3B,C) and a few residues from the DSP-core, account for eleven arginines, all facing the solvent (Fig. 7). We speculate this continuous basic surface clustered on one side of the enzyme could provide an attachment point for highly acidic substrates, such as the phosphorylated p53-TAD and promote substrate recruitment to DUSP26. Since the closed conformation of helix α9 is predicted to pack against helix α7, which is directly continuous to the PTP-loop (Fig. 6A), this interaction may trigger a conformational change in the PTP-loop that mediates its activation. DUSP26 PTP-loop observed crystallographically is in fact closed and tightly coordinated to a water molecule (Fig. 5C). In analogy to the phosphatase MKP-4 (38), which presents a closed conformation of the PTP-loop and has minimal catalytic activity in the absence of substrate (53), substrate binding to DUSP26 may trigger a conformational change that opens up the PTP-loop, thereby marking the transition from an inactive to an active conformation of the phosphatase. The suggested mechanism is distinct from what proposed for VH1 and laforin, where dimerization is thought to be essential for catalytic activity, by generating a binding surface complementary to the phospho-substrate (phosphorylated STAT1 for VH1 (13, 14) and phospho-glycogen (12) for laforin).

Conclusive remarks

Several debilitating human diseases such as cancer, diabetes, inflammation and Alzheimer's disease are intimately linked to DUSPs. Inhibiting DUSPs is a potential therapeutic strategy of great interest in pharmacology (54, 55). Unlike kinases, for which the molecular determinants for substrate specificity are well understood (56), it is unclear how DUSPs selectively recognize their substrates. In this paper, we have described the structural organization of human DUSP26 and characterized its conformational stability and oligomeric state in solution. This work is a step forward toward characterizing DUSP26 composition and biologically active conformation. DUSP26 is indeed a powerful and novel therapeutic target for the treatment of aggressive pediatric malignancy and its inhibition may be of great usefulness to increase neuroblastoma chemosensitivity.

Acknowledgments

We are thankful to Vivian Stojanoff, Marc Allaire and the scientific staff at NSLS beamlines X6A and X29 for assistance and help in data collection.

Funding source

This work was supported in part by NIH grant GM074846-01A1. Research in this publication includes work carried out at the Kimmel Cancer Center X-ray Crystallography and Molecular Interaction Facility, which is supported in part by NCI Cancer Center Support Grant P30 CA56036.

ABBREVIATIONS

DUSP26	Dual Specificity Phosphatase 26
DSP	dual specificity phosphatase
PTP	protein tyrosine phosphatase
TAD	transactivation domain
CD	circular dichroism
AUC	analytical ultracentrifugation
R_H	hydrodynamic radius
***app*T_m**	apparent melting temperature (*app*T_m)
W_{AS}	active site water

REFERENCES

1. Denu JM, Stuckey JA, Saper MA, Dixon JE. Form and function in protein dephosphorylation. Cell. 1996; 87:361–364. [PubMed: 8898189]
2. Zhang ZY. Protein tyrosine phosphatases: structure and function, substrate specificity, and inhibitor development. Annu Rev Pharmacol Toxicol. 2002; 42:209–234. [PubMed: 11807171]
3. Alonso A, Sasin J, Bottini N, Friedberg I, Osterman A, Godzik A, Hunter T, Dixon J, Mustelin T. Protein tyrosine phosphatases in the human genome. Cell. 2004; 117:699–711. [PubMed: 15186772]
4. Ducruet AP, Vogt A, Wipf P, Lazo JS. Dual specificity protein phosphatases: therapeutic targets for cancer and Alzheimer's disease. Annu Rev Pharmacol Toxicol. 2005; 45:725–750. [PubMed: 15822194]
5. Patterson KI, Brummer T, O'Brien PM, Daly RJ. Dual-specificity phosphatases: critical regulators with diverse cellular targets. Biochem J. 2009; 418:475–489. [PubMed: 19228121]
6. Guan KL, Broyles SS, Dixon JE. A Tyr/Ser protein phosphatase encoded by vaccinia virus. Nature. 1991; 350:359–362. [PubMed: 1848923]
7. Phan J, Tropea JE, Waugh DS. Structure-assisted discovery of Variola major H1 phosphatase inhibitors. Acta Crystallogr D Biol Crystallogr. 2007; 63:698–704. [PubMed: 17505108]
8. Jackson MD, Denu JM. Molecular reactions of protein phosphatases--insights from structure and chemistry. Chem Rev. 2001; 101:2313–2340. [PubMed: 11749375]
9. Alonso A, Burkhalter S, Sasin J, Tautz L, Bogetz J, Huynh H, Bremer MC, Holsinger LJ, Godzik A, Mustelin T. The minimal essential core of a cysteine-based protein-tyrosine phosphatase revealed by a novel 16-kDa VH1-like phosphatase, VHZ. J Biol Chem. 2004; 279:35768–35774. [PubMed: 15201283]
10. Maehama T, Taylor GS, Dixon JE. PTEN and myotubularin: novel phosphoinositide phosphatases. Annu Rev Biochem. 2001; 70:247–279. [PubMed: 11395408]
11. Deshpande T, Takagi T, Hao L, Buratowski S, Charbonneau H. Human PIR1 of the protein-tyrosine phosphatase superfamily has RNA 5'-triphosphatase and diphosphatase activities. J Biol Chem. 1999; 274:16590–16594. [PubMed: 10347225]
12. Tagliabracci VS, Turnbull J, Wang W, Girard JM, Zhao X, Skurat AV, Delgado-Escueta AV, Minassian BA, Depaoli-Roach AA, Roach PJ. Laforin is a glycogen phosphatase, deficiency of which leads to elevated phosphorylation of glycogen in vivo. Proc Natl Acad Sci U S A. 2007; 104:19262–19266. [PubMed: 18040046]

13. Koksal AC, Nardozzi JD, Cingolani G. Dimeric quaternary structure of the prototypical dual specificity phosphatase VH1. J Biol Chem. 2009; 284:10129–10137. [PubMed: 19211553]
14. Koksal AC, Cingolani G. Dimerization of Vaccinia Virus VH1 Is Essential for Dephosphorylation of STAT1 at Tyrosine 701. J Biol Chem. 2011; 286:14373–14382. [PubMed: 21362620]
15. Vasudevan SA, Skoko J, Wang K, Burlingame SM, Patel PN, Lazo JS, Nuchtern JG, Yang J. MKP-8, a novel MAPK phosphatase that inhibits p38 kinase. Biochem Biophys Res Commun. 2005; 330:511–518. [PubMed: 15796912]
16. Takagaki K, Shima H, Tanuma N, Nomura M, Satoh T, Watanabe M, Kikuchi K. Characterization of a novel low-molecular-mass dual specificity phosphatase-4 (LDP-4) expressed in brain. Mol Cell Biochem. 2007; 296:177–184. [PubMed: 17001450]
17. Hu Y, Mivechi NF. Association and regulation of heat shock transcription factor 4b with both extracellular signal-regulated kinase mitogen-activated protein kinase and dual-specificity tyrosine phosphatase DUSP26. Mol Cell Biol. 2006; 26:3282–3294. [PubMed: 16581800]
18. Wang JY, Lin CH, Yang CH, Tan TH, Chen YR. Biochemical and biological characterization of a neuroendocrine-associated phosphatase. J Neurochem. 2006; 98:89–101. [PubMed: 16805799]
19. Yu W, Imoto I, Inoue J, Onda M, Emi M, Inazawa J. A novel amplification target, DUSP26, promotes anaplastic thyroid cancer cell growth by inhibiting p38 MAPK activity. Oncogene. 2007; 26:1178–1187. [PubMed: 16924234]
20. Tanuma N, Nomura M, Ikeda M, Kasugai I, Tsubaki Y, Takagaki K, Kawamura T, Yamashita Y, Sato I, Sato M, Katakura R, Kikuchi K, Shima H. Protein phosphatase Dusp26 associates with KIF3 motor and promotes N-cadherin-mediated cell-cell adhesion. Oncogene. 2009; 28:752–761. [PubMed: 19043453]
21. Shang X, Vasudevan SA, Yu Y, Ge N, Ludwig AD, Wesson CL, Wang K, Burlingame SM, Zhao YJ, Rao PH, Lu X, Russell HV, Okcu MF, Hicks MJ, Shohet JM, Donehower LA, Nuchtern JG, Yang J. Dual-specificity phosphatase 26 is a novel p53 phosphatase and inhibits p53 tumor suppressor functions in human neuroblastoma. Oncogene. 2010; 29:4938–4946. [PubMed: 20562916]
22. Cabre F, Canela EI, Canela MA. Accuracy and precision in the determination of Stokes radii and molecular masses of proteins by gel filtration chromatography. J Chromatogr. 1989; 472:347–356. [PubMed: 2777944]
23. Lee WL, Ostap EM, Zot HG, Pollard TD. Organization and ligand binding properties of the tail of Acanthamoeba myosin-IA. Identification of an actin-binding site in the basic (tail homology-1) domain. J Biol Chem. 1999; 274:35159–35171. [PubMed: 10574999]
24. Bhardwaj A, Olia AS, Walker-Kopp N, Cingolani G. Domain organization and polarity of tail needle GP26 in the portal vertex structure of bacteriophage P22. J Mol Biol. 2007; 371:374–387. [PubMed: 17574574]
25. Otwinowski Z, Minor W. Processing of X-ray Diffraction Data Collected in Oscillation Mode. Methods in Enzymology 276: Macromolecular Crystallography. 1997:307–326.
26. McCoy AJ, Grosse-Kunstleve RW, Adams PD, Winn MD, Storoni LC, Read RJ. Phaser crystallographic software. J Appl Crystallogr. 2007; 40:658–674. [PubMed: 19461840]
27. Emsley P, Cowtan K. Coot: model-building tools for molecular graphics. Acta Crystallogr D Biol Crystallogr. 2004; 60:2126–2132. [PubMed: 15572765]
28. Adams PD, Afonine PV, Bunkoczi G, Chen VB, Davis IW, Echols N, Headd JJ, Hung LW, Kapral GJ, Grosse-Kunstleve RW, McCoy AJ, Moriarty NW, Oeffner R, Read RJ, Richardson DC, Richardson JS, Terwilliger TC, Zwart PH. PHENIX: a comprehensive Python-based system for macromolecular structure solution. Acta Crystallogr D Biol Crystallogr. 2004; 66:213–221. [PubMed: 20124702]
29. Murshudov GN, Vagin AA, Dodson EJ. Refinement of macromolecular structures by the maximum-likelihood method. Acta Crystallogr D Biol Crystallogr. 1997; 53:240–255. [PubMed: 15299926]
30. The CCP4 suite: programs for protein crystallography. Acta Crystallogr D Biol Crystallogr. 1994; 50:760–763. [PubMed: 15299374]
31. DeLano, WL. The PyMOL Molecular Graphics System. World Wide Web. 2002. http://www.pymol.org.

32. Dolinsky TJ, Nielsen JE, McCammon JA, Baker NA. PDB2PQR: an automated pipeline for the setup of Poisson-Boltzmann electrostatics calculations. Nucleic Acids Res. 2004; 32:W665–W667. [PubMed: 15215472]
33. Laskowski RA. PDBsum new things. Nucleic Acids Res. 2009; 37:D355–D359. [PubMed: 18996896]
34. Krissinel E, Henrick K. Inference of macromolecular assemblies from crystalline state. J Mol Biol. 2007; 372:774–797. [PubMed: 17681537]
35. Ortega A, Amoros D, Garcia de la Torre J. Prediction of hydrodynamic and other solution properties of rigid proteins from atomic- and residue-level models. Biophys J. 2011; 101:892–898. [PubMed: 21843480]
36. Lountos GT, Tropea JE, Waugh DS. Structure of human dual-specificity phosphatase 27 at 2.38 A resolution. Acta Crystallogr D Biol Crystallogr. 2011; 67:471–479. [PubMed: 21543850]
37. Yuvaniyama J, Denu JM, Dixon JE, Saper MA. Crystal structure of the dual specificity protein phosphatase VHR. Science. 1996; 272:1328–1331. [PubMed: 8650541]
38. Jeong DG, Yoon TS, Jung SK, Park BC, Park H, Ryu SE, Kim SJ. Exploring binding sites other than the catalytic core in the crystal structure of the catalytic domain of MKP-4. Acta Crystallogr D Biol Crystallogr. 2011; 67:25–31. [PubMed: 21206059]
39. Lee CW, Martinez-Yamout MA, Dyson HJ, Wright PE. Structure of the p53 transactivation domain in complex with the nuclear receptor coactivator binding domain of CREB binding protein. Biochemistry. 2010; 49:9964–9971. [PubMed: 20961098]
40. Kruse JP, Gu W. Modes of p53 regulation. Cell. 2009; 137:609–622. [PubMed: 19450511]
41. Levine AJ. p53, the cellular gatekeeper for growth and division. Cell. 1997; 88:323–331. [PubMed: 9039259]
42. Meek DW. Tumour suppression by p53: a role for the DNA damage response? Nat Rev Cancer. 2009; 9:714–723. [PubMed: 19730431]
43. Dornan D, Hupp TR. Inhibition of p53-dependent transcription by BOX-I phospho-peptide mimetics that bind to p300. EMBO Rep. 2001; 2:139–144. [PubMed: 11258706]
44. Dornan D, Shimizu H, Perkins ND, Hupp TR. DNA-dependent acetylation of p53 by the transcription coactivator p300. J Biol Chem. 2003; 278:13431–13441. [PubMed: 12499368]
45. Dornan D, Shimizu H, Burch L, Smith AJ, Hupp TR. The proline repeat domain of p53 binds directly to the transcriptional coactivator p300 and allosterically controls DNA-dependent acetylation of p53. Mol Cell Biol. 2003; 23:8846–8861. [PubMed: 14612423]
46. Tweddle DA, Malcolm AJ, Bown N, Pearson AD, Lunec J. Evidence for the development of p53 mutations after cytotoxic therapy in a neuroblastoma cell line. Cancer Res. 2001; 61:8–13. [PubMed: 11196202]
47. Maclaine NJ, Hupp TR. The regulation of p53 by phosphorylation: a model for how distinct signals integrate into the p53 pathway. Aging (Albany NY). 2009; 1:490–502. [PubMed: 20157532]
48. Moll UM, Ostermeyer AG, Ahomadegbe JC, Mathieu MC, Riou G. p53 mediated tumor cell response to chemotherapeutic DNA damage: a preliminary study in matched pairs of breast cancer biopsies. Hum Pathol. 1995; 26:1293–1301. [PubMed: 8522300]
49. Moll UM, LaQuaglia M, Benard J, Riou G. Wild-type p53 protein undergoes cytoplasmic sequestration in undifferentiated neuroblastomas but not in differentiated tumors. Proc Natl Acad Sci U S A. 1995; 92:4407–4411. [PubMed: 7753819]
50. Vousden KH, Lu X. Live or let die: the cell's response to p53. Nat Rev Cancer. 2002; 2:594–604. [PubMed: 12154352]
51. Liu Y, Wang Y, Wu C, Liu Y, Zheng P. Dimerization of Laforin is required for its optimal phosphatase activity, regulation of GSK3beta phosphorylation, and Wnt signaling. J Biol Chem. 2006; 281:34768–34774. [PubMed: 16971387]
52. Berger P, Schaffitzel C, Berger I, Ban N, Suter U. Membrane association of myotubularin-related protein 2 is mediated by a pleckstrin homology-GRAM domain and a coiled-coil dimerization module. Proc Natl Acad Sci U S A. 2003; 100:12177–12182. [PubMed: 14530412]

53. Camps M, Nichols A, Gillieron C, Antonsson B, Muda M, Chabert C, Boschert U, Arkinstall S. Catalytic activation of the phosphatase MKP-3 by ERK2 mitogen-activated protein kinase. Science. 1998; 280:1262–1265. [PubMed: 9596579]

54. Lazo JS, Wipf P. Phosphatases as targets for cancer treatment. Curr Opin Investig Drugs. 2009; 10:1297–1304.

55. Bakan A, Lazo JS, Wipf P, Brummond KM, Bahar I. Toward a molecular understanding of the interaction of dual specificity phosphatases with substrates: insights from structure-based modeling and high throughput screening. Curr Med Chem. 2008; 15:2536–2544. [PubMed: 18855677]

56. Ubersax JA, Ferrell JE Jr. Mechanisms of specificity in protein phosphorylation. Nat Rev Mol Cell Biol. 2007; 8:530–541. [PubMed: 17585314]

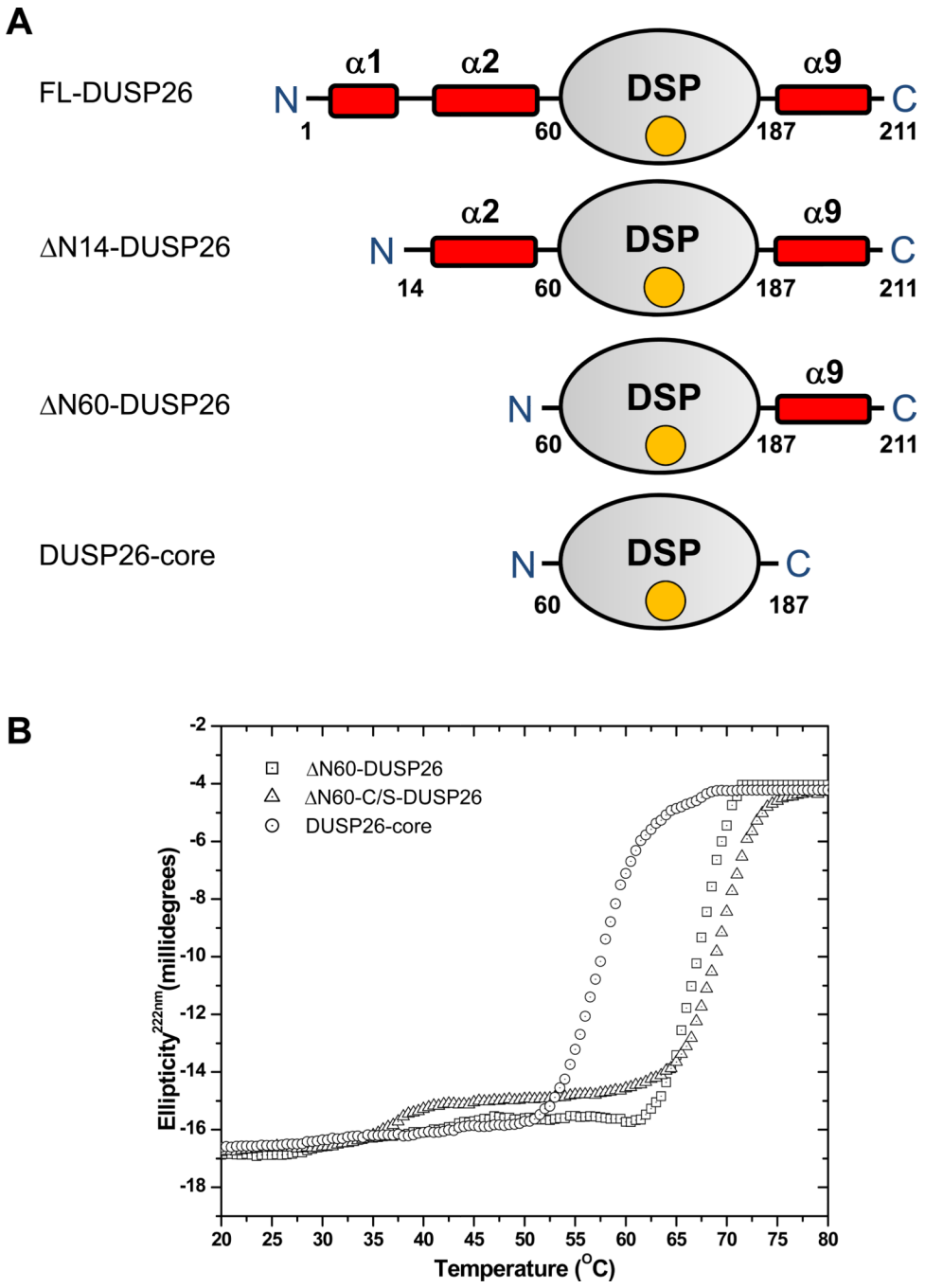

Figure 1. Domain organization and stability of DUSP26

(**A**) Schematic diagram of DUSP26 domain organization and deletion constructs generated in this study. The DSP domain (res. 61–186) is colored in gray and is flanked by two predicted N-terminal α-helices (α1, α2) and a C-terminal helix (α9) (colored in red). (**B**) Stability of DUSP26 against thermal denaturation monitored by measuring changes in the ellipticity intensity at 222 nm as a function of temperature. The concentration of DUSP26 constructs used in this experiment was 10 μM. All T_m*s* measured in this experiment were apparent (*app*T_m*s*) as DUSP26 constructs unfolded irreversibly. A complete list of *app*T_m*s* is in Table 1.

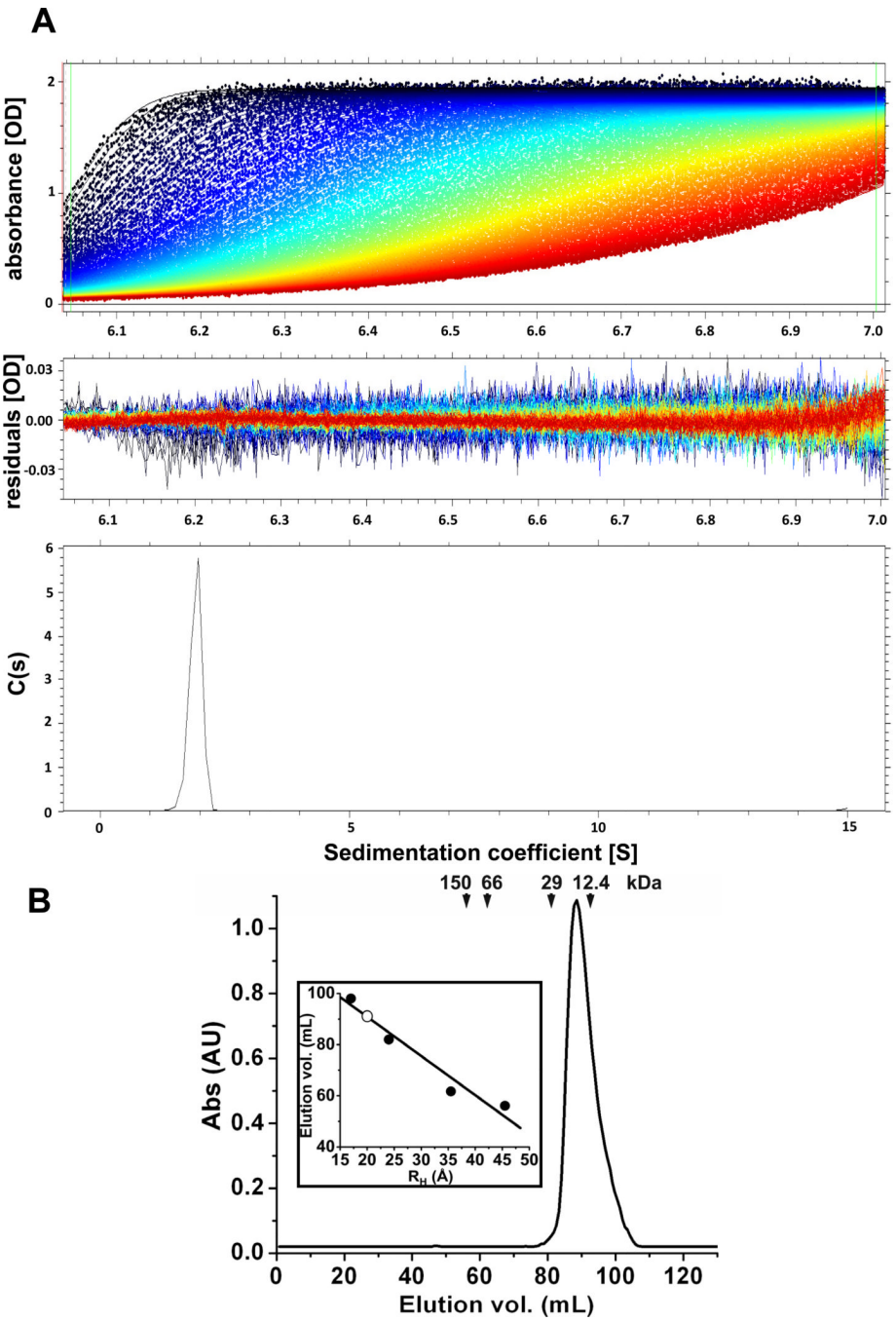

Figure 2. DUSP26 exists as a monomer in solution

(**A**) Sedimentation velocity profiles of ΔN60-C/S-DUSP26 measured in 0.15 M sodium chloride at 20 °C. Top panel: raw absorbance at 278 nm plotted as a function of the radial position. Data at intervals of 20 min are shown as dots for sedimentation at 40,000 rpm. The monophasic sedimentation boundaries suggest that ΔN60-C/S-DUSP26 exists as a single species of homogeneous oligomeric state. Middle panel: the residuals between fitted curve and raw data. Bottom panel: the fitted distribution of the apparent sedimentation coefficient (s*) calculated for ΔN60-C/S-DUSP26 is 1.925S (and $s_{20,w}$=2.012S) corresponds to an estimated molecular mass of ~18.1kDa, consistent with a monomer. A complete list of hydrodynamic parameters is in Table 1. (**B**) Gel filtration analysis of purified ΔN60-C/S-

DUSP26. The Superdex 75 gel filtration column was calibrated using molecular weight markers, whose elution volumes and relative molecular weights are indicated by arrows. ΔN60-C/S-DUSP26 eluted after 91 ml, consistent with a monomeric species of a ~20 kDa. The insert panel shows a calibration curve obtained by plotting elution volumes of molecular markers (in ml) versus known hydrodynamic radii (R_H) (shown as filled circles). The hydrodynamic radius of ΔN60-C/S-DUSP26 estimated from this calibration (open circle) is R_H ~21.0 Å (Table 1).

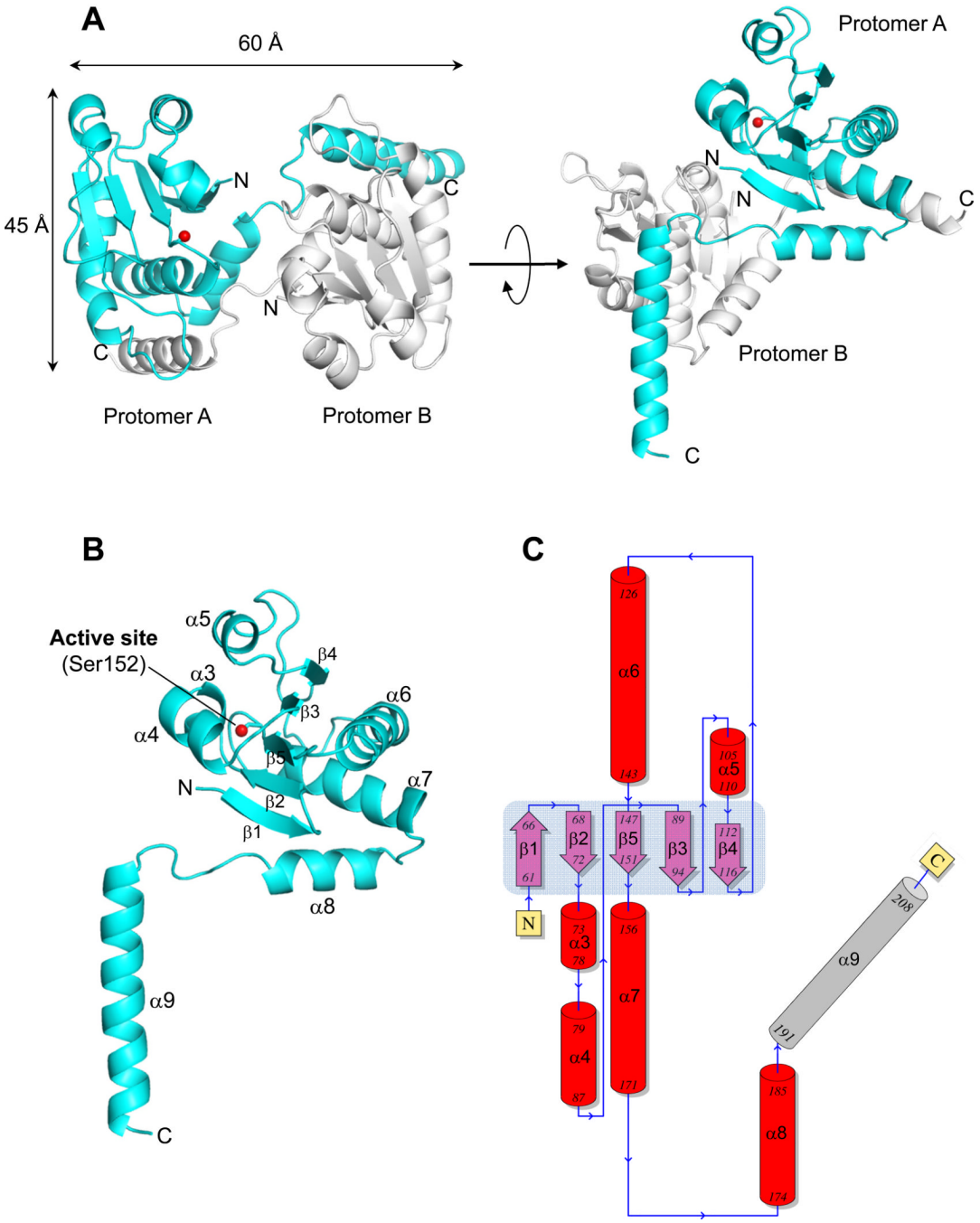

Figure 3. Atomic structure of ΔN60-C/S-DUSP26 at 1.68 Å resolution

(**A**) Ribbon diagram of ΔN60-C/S-DUSP26 crystallographic dimer (in side and top view) that is present in two copies in the asymmetric unit. Two protomers of a dimer (referred to as A and B) are colored in cyan and gray, respectively. The position of protomer A catalytic residue (Ser152) is shown as a red ball. (**B**) Ribbon diagram of protomer A showing all secondary structure element. (**C**) Topological diagram of ΔN60-C/S-DUSP26 protomer A with α-helices and β-strands forming the DSP-core colored in red and purple, respectively and the domain swapped helix α9 in gray. The central β-sheet formed by strands β1–β5 is highlighted in light blue. A complete list of crystallographic parameters is in Table 2.

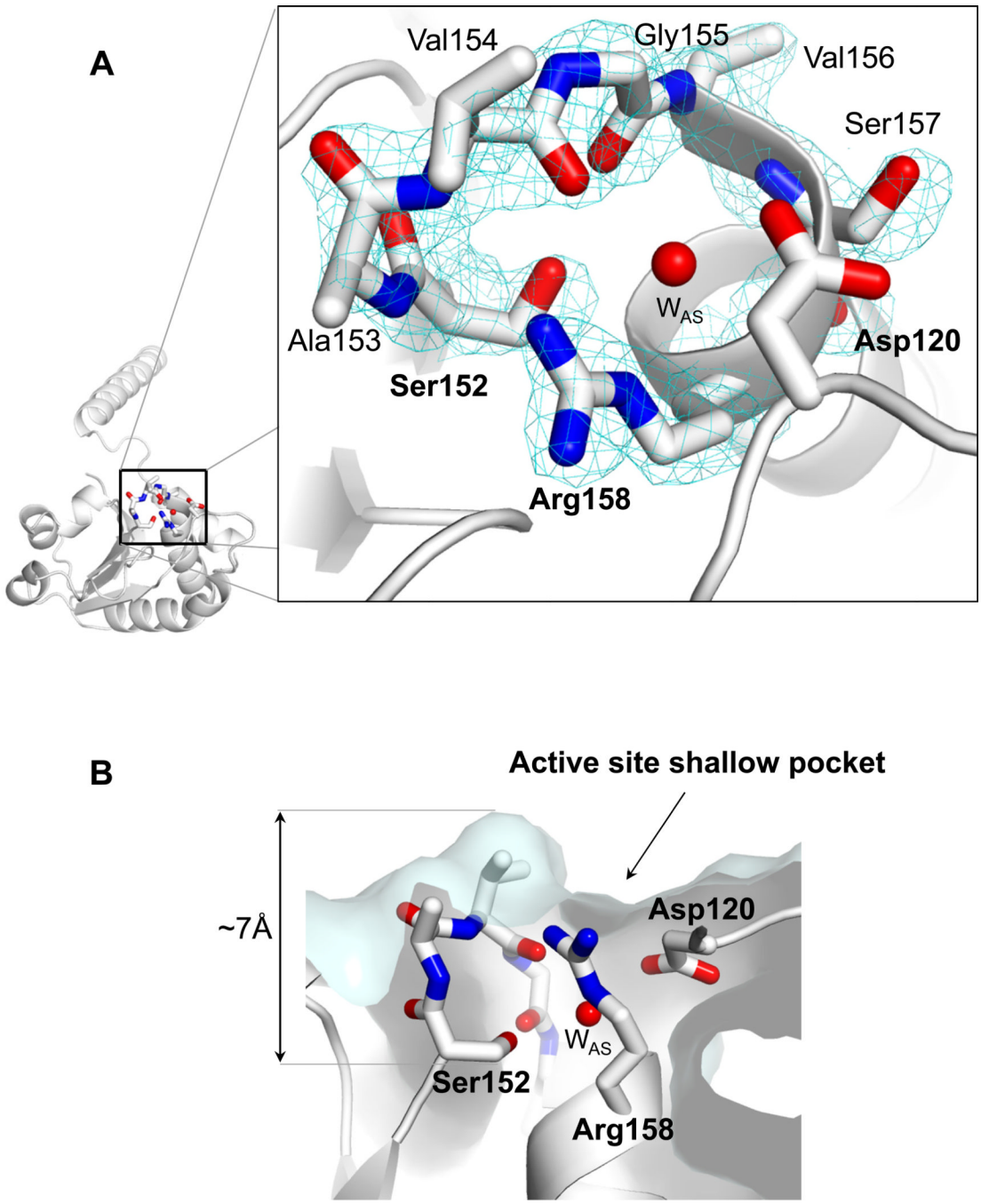

Figure 4. Architecture of DUSP26 active site

(**A**) Magnified view of ΔN60-C/S-DUSP26 active site visualized at 1.68 Å resolution. The final 2Fo − Fc electron density map contoured at 1.5 σ above background (cyan) is displayed around the refined model of ΔN60-C/S-DUSP26 PTP-loop (shown as sticks). Residues forming the catalytic loops are labeled. (**B**) Cut-through view of DUSP26 catalytic pocket reveals the location of Ser152, which is buried from the solvent ~7 Å below the enzyme surface.

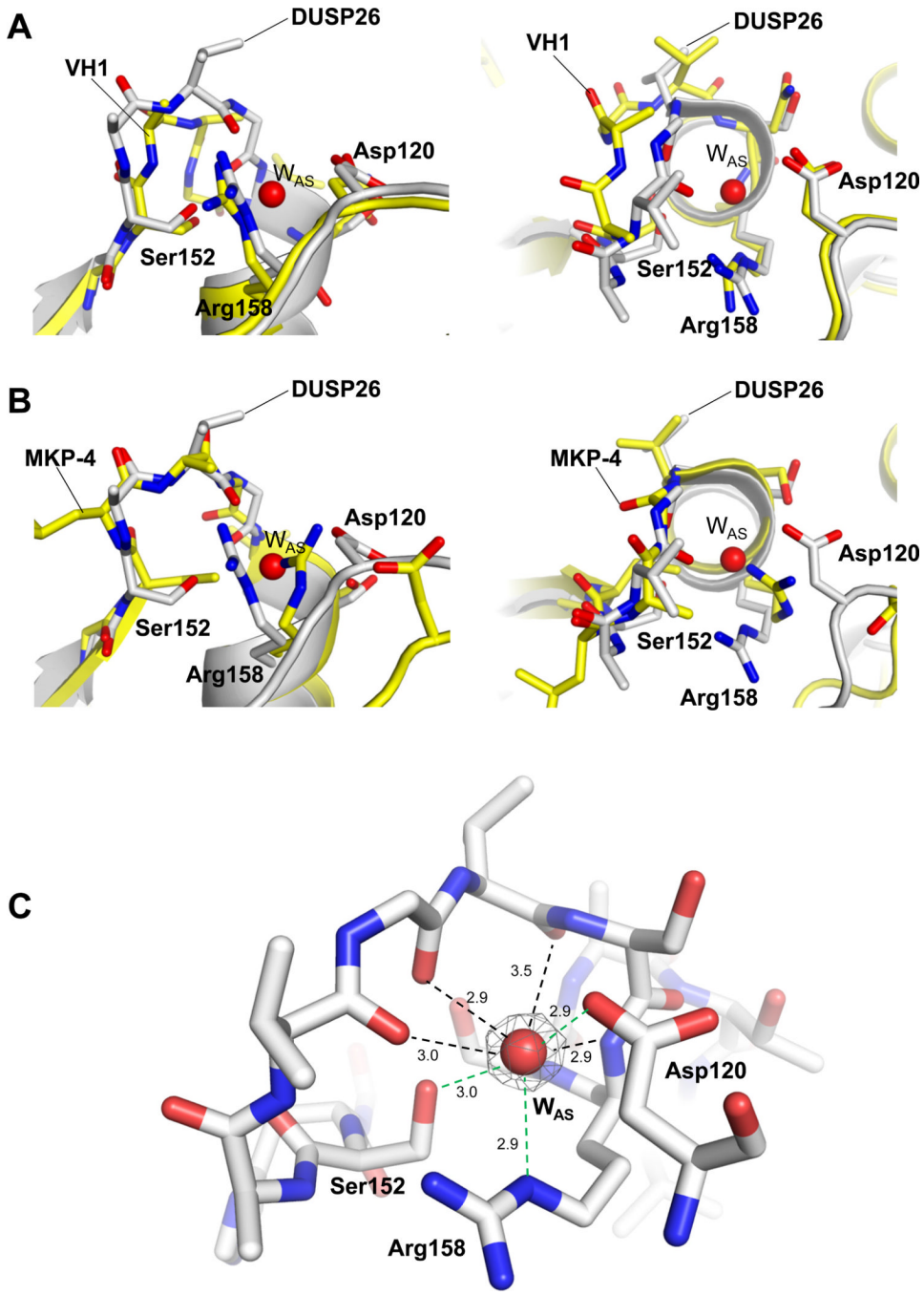

Figure 5. Conformation of DUSP26 PTP-binding loop

Superimposition of ΔN60-C/S-DUSP26 PTP-loop with VH1 (pdb id 3CM3) (**A**) and MKP-4 (pdb id 3LJ8) (**B**), in side (*left panels*) and top view (*right panels*). In all panels, DUSP26 is colored in gray while VH1 and MKP-4 are in yellow. For clarity, only DUSP26 catalytic triad and W_{AS} have been labeled (and the phosphate ion trapped in VH1 active site has been omitted). (**C**) Snapshot of ΔN60-C/S-DUSP26 W_{AS} (red sphere) trapped inside the PTP-loop (shown as sticks). A Fo − Fc electron density map (colored in gray) contoured at 3.5 σ above background is overlaid to W_{AS}. The density was calculated after omitting W_{AS}

from the refined model. Distances between W_{AS} and PTP-loop main and side chain atoms are indicated by black and green dashed lines, respectively.

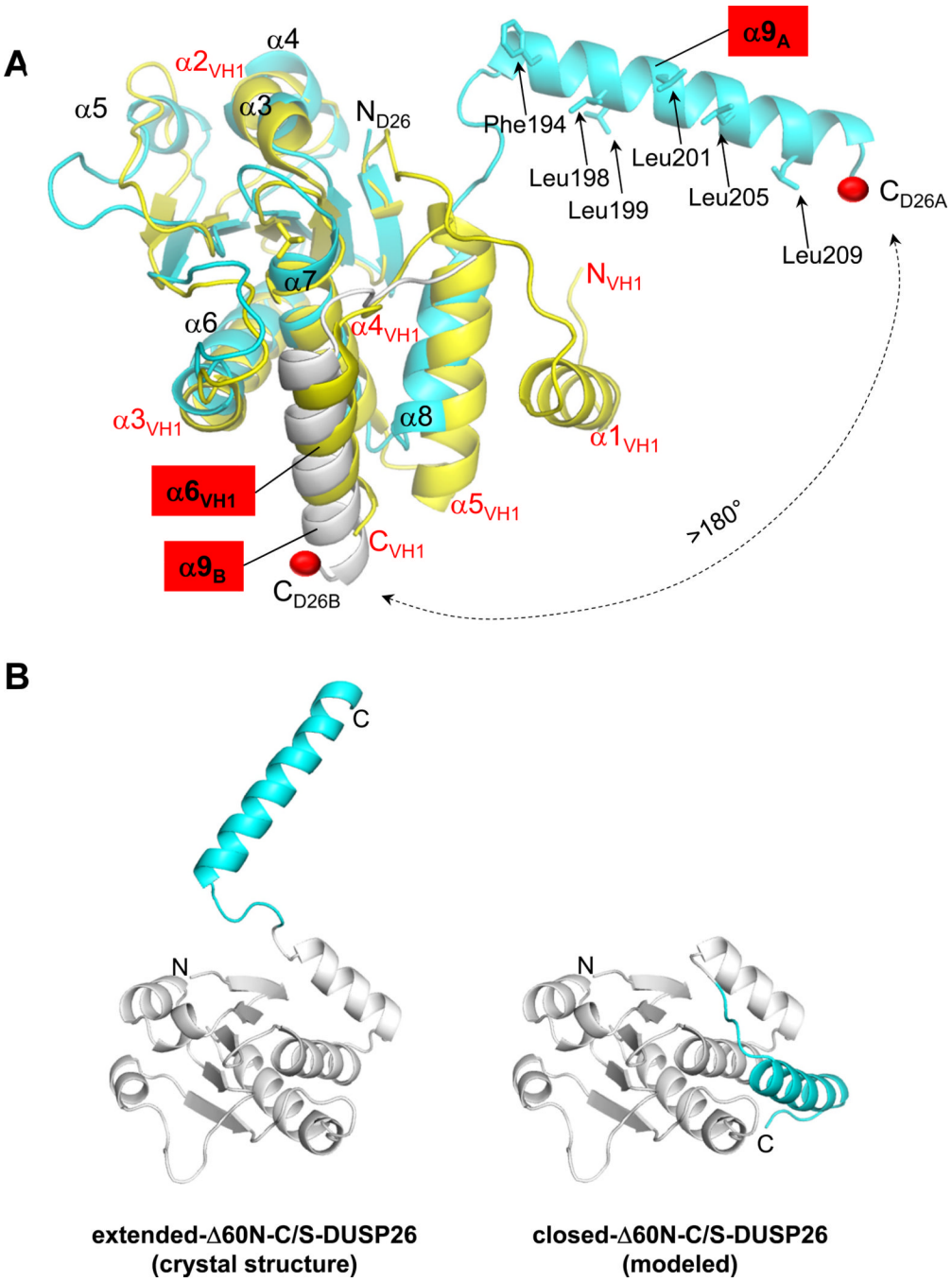

Figure 6. Flexibility of DUSP26 C-terminal helix α9

(**A**) Superimposition of ΔN60-C/S-DUSP26 with VH1 (colored in cyan and yellow, respectively). For clarity, only α-helices are labeled; helix α9, and its counterpart in VH1, helix $\alpha6_{VH1}$ are highlighted in red. Hydrophobic residues protruding on the surface of helix α9 are shown as sticks and their position indicated by arrows. Helix α9 of protomer B ($\alpha9_B$) is shown as a gray ribbon. A red ball indicates the position of DUSP26 $\alpha9_A$ and $\alpha9_B$ C-termini; a dashed arrow illustrates the putative trajectory of the conformational change helix α9 would undergo from the position observed crystallographically to that adopted by helix $\alpha6_{VH1}$ in VH1 (or helix $\alpha9_B$ in protomer B). (**B**) Ribbon diagram of ΔN60-C/S-DUSP26

protomer observed crystallographically, with helix α9 in an extended conformation (‘extended-ΔN60-C/S-DUSP26’), and of a model of ΔN60-C/S-DUSP26 with helix α9 packed against the DSP-core like in VH1 (‘closed-ΔN60-C/S-DUSP26’). In both diagrams, the DSP-core is colored in gray and helix α9 is in cyan.

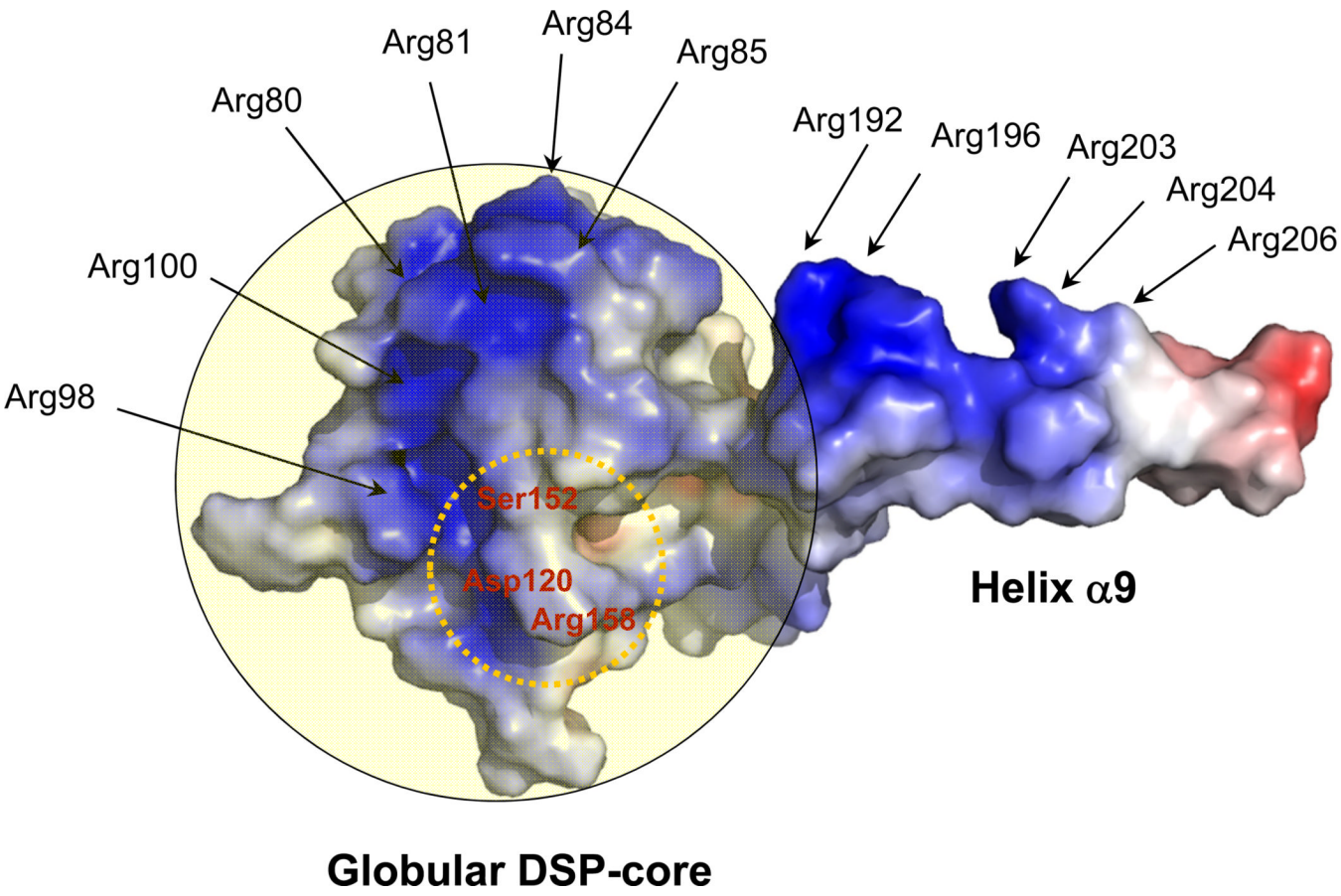

Figure 7. Electrostatic surface potential of ΔN60-C/S-DUSP26

Arginines exposed on the surface of ΔN60-C/S-DUSP26 (mainly helices α9 and α4) are shown by arrows. The DSP-core is overlaid to a semi-transparent yellow circle. Active site residues are circled by a dashed yellow line.

TABLE 1

Biophysical parameters measured by CD, AUC and gel filtration chromatography to study DUSP26 conformational stability and oligomeric state.

Protein	Apparent Tm (°C)	Apparent Sedimentation coef, s* (S)	Standardized Sedimentation coef, $s_{20,W}$ (S)	Frictional ratio (f/f_0)	Hydo-dynamic radius, R_H (Å)*	Calculated mass (kDa)	Theoretical mass (kDa)**
ΔN60-DUSP26	68	1.925	2.012	1.23	22.7/21.0	18.1	18.2
ΔN60-C/S-DUSP26	69	1.922	2.007	1.23	22.7/21.0	18.1	18.2
DUSP26-CORE	59	1.811	1.948	1.20	20.2/20.0	16.6	15.4

*Hydrodynamic radius from AUC / Gel Filtration

**Theoretical mass includes additional C-terminal residues introduced by cloning (‘GLEALEHHHHHH’)

TABLE 2

Crystallographic data collection and refinement statistics.

Data collection statistics	
Wavelength (Å)	0.9789
Space group	P212121
Unit cell dimensions (Å)	*a*=81.9, *b*=82.3, *c*=91.7
Angles (°)	α=β=γ=90
Resolution range (Å)	15-1.68
Wilson *B*-factor (Å^2)	20.0
Total observations	754,413
Unique observations	69,003
Completeness (%)	96.3 (97.7)
R_{sym}[a] (%)	5.0 (55.3)
<I>/<σ(I)>	40.2 (3.8)
Refinement statistics	
Number of reflections (10-1.68 Å)	64,739
R_{work}/R_{free}[b] (%)	18.5/21.5
Number copies in asym unit	4
Number of water molecules	491
B value of model (Å^2) chains A / B / C / D / Waters	32.1 / 27.9 / 44.2 / 43.2 / 41.1
r.m.s. deviation from ideal bond length (Å) / angles (°)	0.006 / 1.0
Ramachandran plot (%) core / allowed / generously allowed / disallowed	95.5 / 4.5 / 0.0 /0.0

The numbers in parenthesis refer to the statistics for the outer resolution shell: (1.74-1.68 Å).

[a] Rsym =Σi,h | I(i,h) – <I(h)> | /$\Sigma_{i,h}$ | I(i,h) | where I(i,h) and <I(h)> are the ith and mean measurement of intensity of reflection h.

[b] The R_{free} value was calculated using 3,540 randomly chosen reflections.